Available online at www.sciencedirect.com
ScienceDirect
Journal of Hazardous Materials 155 (2008) 572–579
Journal of Hazardous Materials
www.elsevier.com/locate/jhazmat

Preparation of Fe^{3+}-doped TiO_2 catalysts by controlled hydrolysis of titanium alkoxide and study on their photocatalytic activity for methyl orange degradation

Tianzhong Tong [a], Jinlong Zhang [a,*], Baozhu Tian [a], Feng Chen [a], Dannong He [b]

[a] *Lab for Advanced Materials and Institute of Fine Chemicals, East China University of Science and Technology, 130 Meilong Road, Shanghai 200237, PR China*

[b] *Shanghai National Engineering Research Center for Nanotechnology, 245 Jiachuan Road, Shanghai 200237, PR China*

Received 4 September 2007; received in revised form 5 November 2007; accepted 25 November 2007
Available online 3 December 2007

Abstract

Fe^{3+}-doped TiO_2 (Fe–TiO_2) porous microspheres were prepared by controlled hydrolysis of $Ti(OC_4H_9)_4$ with water generated "in situ" via an esterification reaction between acetic acid and ethanol, followed by hydrothermal treatment. The samples were characterized by X-ray diffraction (XRD), transmission electron microscopy (TEM), atomic absorption flame emission spectroscopy (AAS), electron paramagnetic resonance (EPR) spectrum, X-ray photoelectron spectroscopy (XPS), UV–vis diffuse reflectance spectroscopy (DRS), and nitrogen adsorption–desorption methods. All of the undoped TiO_2 and Fe–TiO_2 samples exclusively consist of primary anatase crystallites, which further form porous microspheres with diameters ranging from 150 to 500 nm. The photocatalytic activity of Fe–TiO_2 catalysts was evaluated from the photodegradation of methyl orange (MO) aqueous solution both under UV and visible light irradiation. Fe^{3+} doping effectively improves the photocatalytic activity under both UV light irradiation and visible light irradiation with an optimal doping concentration of 0.1 and 0.2%, respectively. The photocatalytic mechanisms of Fe–TiO_2 catalysts were tentatively discussed.

Keywords: Anatase; Visible light; Photodegradation; Esterification reaction; Fe^{3+} doping

1. Introduction

Since the discovery of photoelectrochemical splitting of water on *n*-TiO_2 electrodes [1], TiO_2-based photocatalysis has attracted extensive interest owing to its great advantages in the complete mineralization of organic pollutants in waste water and air. As a popular photocatalyst, TiO_2 has been widely studied because of its various merits, such as optical-electronic properties, low-cost, chemical stability, and non-toxicity [2,3]. However, it is unavoidable to face two issues for its practical applications, one of which is to improve the low photo-quantum efficiency of TiO_2 that arises from the fast recombination of photo-generated electrons and holes; another is to further extend its photoresponse into visible light regions. Particularly, TiO_2 can only be activated by UV light due to its large band gap (E_{bg}, anatase ≈ 3.2 eV, E_{bg}, rutile ≈ 3.0 eV) and only make use of 3–5% of the solar spectrum that reach the earth [4,5]. Thus, it is necessary to develop a proficient way to not only extend the absorbance of TiO_2 into visible regions but also reduce the recombination of photo-generated electrons and photo-generated holes. Recently, some studies have reported doping with suitable transitional metals is a useful way for improving the above two performances of TiO_2 [5–10]. Amongst a variety of transitional metals, iron has been considered to be an appropriate candidate due to the fact that the radium of Fe^{3+} (0.69 A) is similar to that of Ti^{4+} (0.745 A), so Fe^{3+} can be easily incorporated into the crystal lattice of TiO_2 [11]. Furthermore, Fe^{3+} can provide a shallow trap for photo-generated electron and hole because the energy level of Fe^{2+}/Fe^{3+} lies close to that of Ti^{3+}/Ti^{4+}, favoring the separation of photo-generated electron-hole pair, and consequently resulting in the improvement of quantum yield [5,11].

Up to now, many methods such as sol–gel [12], hydrothermal [6], wet impregnation [13], ion-implantation [5], and metal

* Corresponding author. Tel.: +86 21 64252062; fax: +86 21 64252062.
E-mail address: jlzhang@ecust.edu.cn (J. Zhang).

0304-3894/$ – see front matter © 2007 Elsevier B.V. All rights reserved.
doi:10.1016/j.jhazmat.2007.11.106

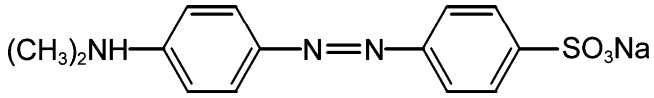

Scheme 1. Molecular structure of MO.

organic chemical vapor deposition (MOCVD) [7] have been established for the preparation of Fe–TiO_2 catalysts. Among these preparation techniques, the relatively simple sol–gel method is the most widely used. However, the morphology of Fe–TiO_2 prepared with this technique is often irregular. Furthermore, the sol–gel-derived precipitates are usually amorphous in nature, which requires further heat treatment to induce crystallization. Unfortunately, the calcination process frequently gives rise to particle agglomeration and grain growth, which is unfavorable for the acquisition of high activity [1].

In this work, Fe–TiO_2 porous microspheres were prepared by excellent controlling the hydrolysis of $Ti(OC_4H_9)_4$ via an esterification reaction between acetic acid and ethanol (Eq. (1)), followed by hydrothermal treatment. The prepared samples have been characterized by XRD, TEM, EPR, XPS, AAS, UV–vis DRS, and nitrogen adsorption–desorption methods. The photodegradation of methyl orange (MO, Scheme 1) dye was chosen as a probe reaction to measure the photocatalytic activity of different samples. Photocatalytic mechanisms for Fe–TiO_2 catalysts under UV light irradiation and visible light irradiation were also tentatively discussed.

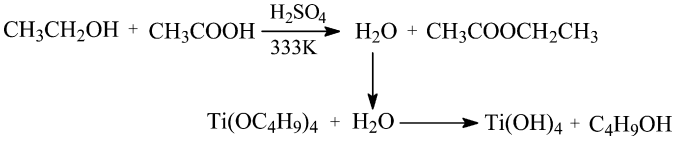

(1)

2. Experimental

2.1. Materials

The chemicals used in this study were titanium tetrabutoxide ($Ti(OC_4H_9$-$n)_4$, 98%, Lingfeng Chemical reagent Co., Ltd., China) as a titanium precursor, iron(III) nitrate ($Fe(NO_3)_3{\cdot}9H_2O$, 99%, Shanghai Chemical Reagent Co., China) as Fe source, anhydrous ethanol (C_2H_5OH, 99.7%, Jiuyi Chemical Reagent Co. Ltd., China), glacial acetic acid (HAc, 99.5%, Shanghai Jinghua Sci. & Tech. Institute, China), concentrated sulfuric acid (H_2SO_4, 98%, Shanghai Jinghua Sci. & Tech. Institute, China).

2.2. Experimental procedure

The synthetic procedure was as follows: under magnetic stirring, 20 ml HAc was added dropwise to a flask containing 10 ml of $Ti(OC_4H_9$-$n)_4$ diluted in 30 ml C_2H_5OH, followed by addition of 1 ml H_2SO_4 and a specific amount of $Fe(NO_3)_3{\cdot}9H_2O$. Then, the obtained clear liquid was sonicated in an ultrasonic cleaning bath (Elma, T660/H, 35 kHZ, 360 W) at 313 K for 1 h and 333 K for 3 h, resulting in the formation of a milk-like sol, which was further transferred into a 100 ml Teflon-inner-liner stainless autoclave and kept at 393 K for 13 h. The resulting precipitates were separated from the mother liquor by centrifugation, washed thoroughly with deionized water and ethanol three times, respectively, and then dried at 373 K in air for 12 h. Finally, the obtained powders were calcined at 733 K for 2 h and designated as x% Fe–TiO_2, where x stands for the mass percentage of Fe in theoretical product. The undoped TiO_2 were prepared by the same procedure, except no $Fe(NO_3)_3{\cdot}9H_2O$ was added.

2.3. Characterization

The phases and crystallite sizes of the prepared samples were characterized by X-ray diffraction (XRD), performed on a Rigaku D/max 2550 VB/PC X-ray diffractometer at room temperature. The patterns were recorded over the angular range 10–80° (2θ), using a scan rate of 2°/min and Cu Kα radiation ($\lambda = 0.154056$ nm) with working voltage and current of 40 kV and 100 mA, respectively. The content of Fe in Fe–TiO_2 samples was determined by atomic absorption flame emission spectroscopy (AAS) (Shimadzu AA-6400F). Transmission electron microscopy (TEM) measurements were performed on a JEOL JEM-100 CX II transmission electron microscopy, operated at an acceleration voltage of 100 kV. The X-band electron paramagnetic resonance (EPR) spectra were recorded at 293 K using a Bruker ER 200D-SRC EPR spectrometer. The instrument employed for XPS studies was a PerkinElmer PHI 5000C ESCA system with Al Kα radiation operated at 250 W. The shift of the binding energy due to relative surface charging was corrected using the C 1s level at 285.0 eV as an internal standard. UV–vis diffuse reflectance spectra (DRS) were obtained using a scan UV–vis-NIR spectrophotometer (Varian Cary 500) equipped with an integrating sphere assembly, using polytetrafluoroethylene as a reference material. The Brunauer–Emmett–Teller (BET) specific surface areas (S_{BET}) of the samples were determined by using nitrogen adsorption in a Micromeritics ASAP 2010 nitrogen-adsorption apparatus. All the samples were degassed at 473 K prior to the measurements. The desorption isotherm was used to determine the pore-size distribution via the Barret–Joyner–Halender (BJH) method.

2.4. Photocatalytic activity measurement

Photodegradation reactions were carried out using a homemade setup, for which the lamp was cooled with flowing water in a quartz cylindrical jacket around the lamp, and a fanner was fixed to maintain a constant temperature during the photocatalytic reaction. UV light and visible light irradiations were achieved using a 300 W high-pressure Hg lamp and halogen–tungsten lamp with UV cut-off filter, respectively. For each test, 0.05 g of catalyst sample was suspended into a 70 ml quartz tube containing 50 ml MO. The concentrations of MO used for UV and visible light irradiation were 30 and 20 mg/l, respectively. The concentration of the catalyst in dye aqueous solution was 1 g/l. After sonicated for 10 min, the pH value of

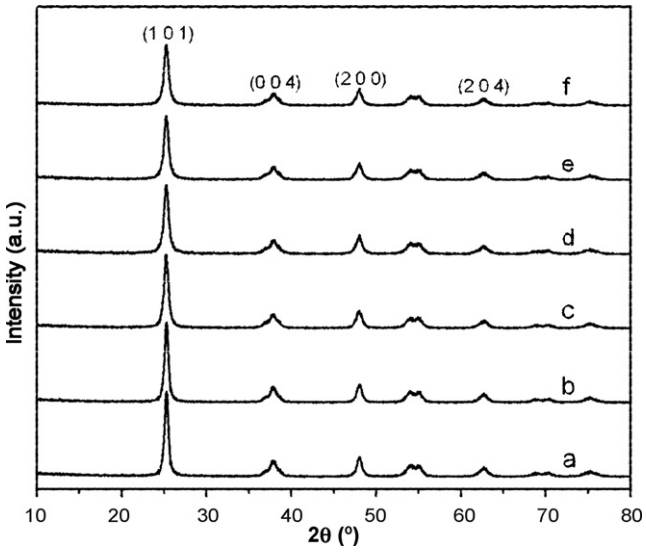

Fig. 1. XRD patterns of (a) TiO_2, (b) 0.05% Fe–TiO_2, (c) 0.1% Fe–TiO_2, (d) 0.2% Fe–TiO_2, (e) 0.4% Fe–TiO_2, and (f) 0.6% Fe–TiO_2.

the suspension was adjusted to 3.5 with 0.1 M HCl. Then, the above suspension was stirred in the dark for 30 min to attain the adsorption–desorption equilibrium for MO and dissolved oxygen on the surface of TiO_2. Subsequently, the obtained suspensions were illuminated with UV or visible light under magnetic stirring. The distance between the light and the reaction tube was fixed at 24 cm. After every given irradiation time, a sample of 3.5 ml suspension was withdrawn, centrifugated and filtered. The residual concentration of MO in the solution was measured with a UV–vis spectrophotometer (Varian Cary 100) at 464 nm, which is the maximum absorption of MO.

3. Results and discussion

3.1. X-ray diffraction analysis

XRD was used to investigate the phase structure and the phase composition of TiO_2 catalysts. Fig. 1 shows the XRD patterns of undoped TiO_2 and Fe–TiO_2 samples. As shown in Fig. 1, all of the samples consist of anatase as a unique phase (JCPDS, No. 21-1272). The peaks at scattering angles of 25.24°, 36.98°, 48.02° and 62.74° correspond to the reflections from the (1 0 1), (0 0 4), (2 0 0) and (2 0 4) crystal planes, respectively, of anatase TiO_2. The average crystallite size of anatase in the different Fe–TiO_2 samples can be calculated by applying the Debye–Scherrer formula [14] on the anatase (1 0 1) diffraction peaks:

$$D = \frac{K\lambda}{\beta \cos\theta}$$

where D is the average crystallite size, K the constant which is taken as 0.89 here, λ the wavelength of the X-ray radiation (Cu Kα = 0.154056 nm), β the corrected band broadening (full width at half-maximum (FWHM)) after subtraction of equipment broadening, and θ is the diffraction angle. The calculated average crystallite sizes for samples undoped TiO_2, 0.05% Fe–TiO_2, 0.1% Fe–TiO_2, 0.2% Fe–TiO_2, 0.4% Fe–TiO_2, and 0.6% Fe–TiO_2 were 15.1, 14.9, 14.5, 14.2, 13.8, and 13.3 nm, respectively (Table 1). This result reveals that doping Fe^{3+} decreases the crystal size of TiO_2, similar to those described by other investigators [6,15]. When Fe^{3+} ions are incorporated into crystal lattice of TiO_2, some extent deformation will be introduced into the crystal lattice of TiO_2 due to the different atomic sizes between Fe^{3+} (0.69 A) and Ti^{4+} (0.745 A). As a result of crystal lattice deformation, the crystallite growth of Fe–TiO_2 grains is restrained during the hydrothermal treatment, resulting in the decrease of the crystal size of TiO_2. In addition, it is noteworthy that no crystalline phase attributed to iron oxide can be found in the XRD patterns. There are two reasons responsible for this result. One possible reason is that the Fe^{3+} content in the Fe–TiO_2 samples is below the detection limit of this technique. Another is that all Fe^{3+} ions might substitute Ti^{4+} ions and insert into the crystal lattice of TiO_2 because the radii of Ti^{4+} and Fe^{3+} ions are very similar [16,17].

3.2. TEM and N_2 adsorption–desorption analysis

Fig. 2 shows the TEM images of undoped TiO_2 (Fig. 2a and e), 0.1% Fe–TiO_2 (Fig. 2b), 0.2% Fe–TiO_2 (Fig. 2c and f), and 0.4% Fe–TiO_2 (Fig. 2d). As shown in Fig. 2(a–d), the morphologies for these samples have no evident differences and all

Table 1
Physicochemical properties and photocatalytic activities of samples prepared

Sample	Crystal phase	Crystal size[a]	S_{BET} (m^2/g)	Fe content[b] (wt%)	UV-degraded MO (%)[c]	Vis-degraded MO (%)[d]
Undoped TiO_2	Anatase	15.1	97	0	63	54
0.05% Fe–TiO_2	Anatase	14.9	96	0.042	71	59
0.10% Fe–TiO_2	Anatase	14.5	102	0.074	79	61
0.15% Fe–TiO_2	Anatase	14.5	105	0.12	69	69
0.20% Fe–TiO_2	Anatase	14.2	110	0.17	58	72
0.3% Fe–TiO_2	Anatase	14.1	108	0.22	43	63
0.40% Fe–TiO_2	Anatase	13.7	117	0.31	36	50
0.60% Fe–TiO_2	Anatase	13.2	122	0.46	24	49
P25	Anatase/rutile	–	49	0	70	56

[a] Calculated by Debye–Scherrer formula.
[b] Determined by atomic absorption flame emission spectroscopy (AAS).
[c] After photodegradation for 1 h, exclusive of equilibrium adsorption for 1 h.
[d] After photodegradation for 6 h, exclusive of equilibrium adsorption for 1 h.

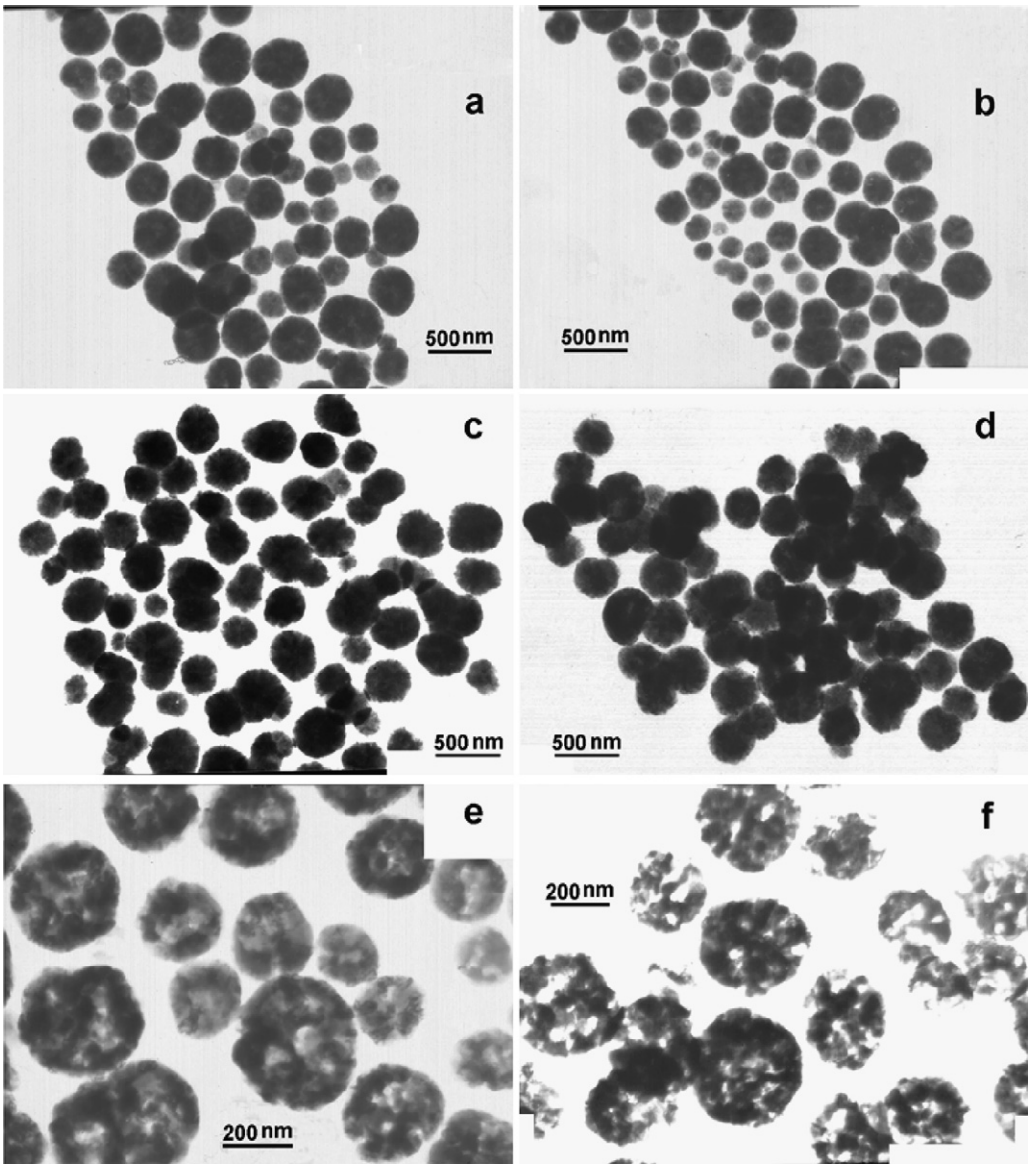

Fig. 2. TEM images of undoped TiO_2 (a and e), 0.1% Fe–TiO_2 (b), 0.2% Fe–TiO_2 (c and f), and 0.4% Fe–TiO_2 (d).

samples consist of spherical particles in sizes varying from 150 to 500 nm. The sizes of spheroids observed in Fig. 2(a–d) are extremely different from the XRD calculated sizes, indicating that each spherical particle observed with TEM is not a single crystallite but the agglomerates of many single crystallites. From Fig. 2e and f, it can be clearly seen that the spheroids observed in Fig. 2a and c consist of primary particles and contain wormhole-like pores.

N_2 adsorption–desorption measurements indicate that mesoporous structure was present for all of the undoped TiO_2 and Fe–TiO_2 samples. The N_2 adsorption–desorption isotherm of the undoped TiO_2, as a representative curve, is shown in Fig. 3. The isotherm is of classical type IV, suggesting the presence of mesopores [18]. A hysteresis loop with a sloping adsorption branch and a relatively sharp steep desorption branch is observed at a relative pressure range of 0.4–0.9, characteristic of H_2 type hysteresis loop [18]. The pore-size distribution curve of the undoped TiO_2 is shown in the inset of Fig. 3. A narrow pore-size distribution with the average pore diameter of 4.3 nm is found. It is worth mentioned that N_2 adsorption–desorption analysis cannot provide the macroporous information of the TiO_2 microspheres. Combined the TEM result, it is reasonable to think the presence of macro-/mesoporous structure should facilitate the pass of reactants and products and consequently favor the improvement of photocatalytic activity. The BET surface areas (S_{BET}) for all the undoped TiO_2 and Fe–TiO_2 were listed in Table 1. It was found that the S_{BET} increases with increasing the Fe doping amount. Compared with undoped TiO_2, the final increased surface area of Fe-doped TiO_2 should be related to the decreased particle size, resulting from Fe dopant.

Enlightened by the previous explanations for the formation of hierarchical macro-/mesoporous structures [19–22], a possible formation mechanism was proposed to account for the formation of TiO_2 porous spheres. Firstly, the hydrolysis reaction of

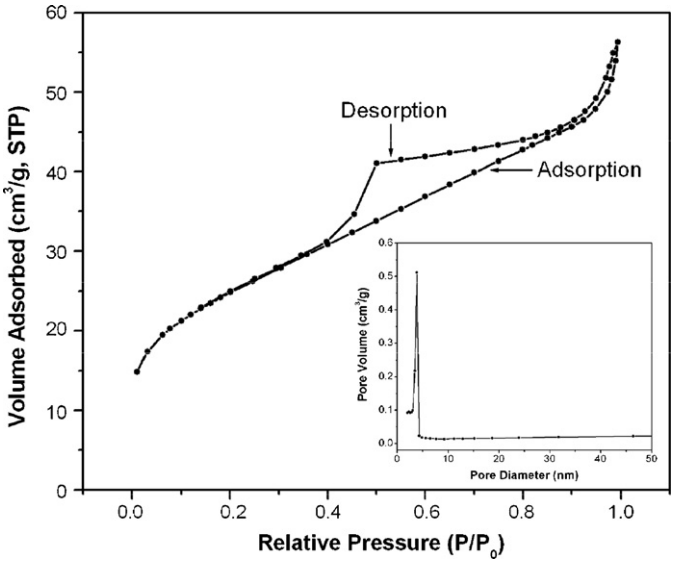

Fig. 3. N_2 adsorption–desorption isotherms and BJH pore size distribution (inset) of the undoped TiO_2.

$Ti(OC_4H_9)_4$ gradually occurs with the generation of "in situ" water derived from the esterification reaction between ethanol and acetic acid. Due to the fact that little water is present at first, the hydrolysis rate occurs slowly, resulting in the formation of microspheres. With the progress of the esterification reaction between ethanol and acetic acid, more and more water molecules will form, which gather together lead to the formation of larger water/ethanol macrochannels at regions both within and near the surface of the microspheres. Meanwhile, the polymerization generates large amounts of TiO_2 spherical particles. The self-aggregation of these spherical particles forms the interparticular mesoporosity.

3.3. EPR and XPS analysis

EPR is a highly sensitive spectroscopic technique for examining paramagnetic species and can give valuable information about the lattice site in which a paramagnetic dopant ion is located. This highly sensitive technique can detect down to 0.01% of iron ions in metal oxide matrices [23]. The EPR spectra of 0.1% Fe–TiO_2, 0.2% Fe–TiO_2, and 0.4% Fe–TiO_2 are shown in Fig. 4a–c, respectively. As shown in Fig. 4, all of the three samples show intense signal at $g = 1.99$ and very weak signal at $g = 4.22$. According to the previous reports [24,25], these two signals should be attributed to Fe^{3+} substituted for Ti^{4+} in the TiO_2 lattice ($g = 1.99$) and to Fe^{3+} substituted in the lattice adjacent to a charge-compensating oxide anion vacancy ($g = 4.22$), respectively. The intensity of EPR signal increases with increasing Fe^{3+} content. According to the previous reports [26–28], Fe^{3+} ions can uniformly distribute within TiO_2 and form stable solid solutions. The analysis of EPR results confirm that Fe^{3+} ions are successfully incorporated into the crystal lattice of TiO_2 with the present preparation method.

Fig. 5 shows the XPS spectrum of Fe 2p peak of sample 0.4% Fe–TiO_2. The binding energy at 711.6 eV should be assigned to $2p_{3/2}$ of Fe^{3+}. This datum exhibits a positive shift compared to

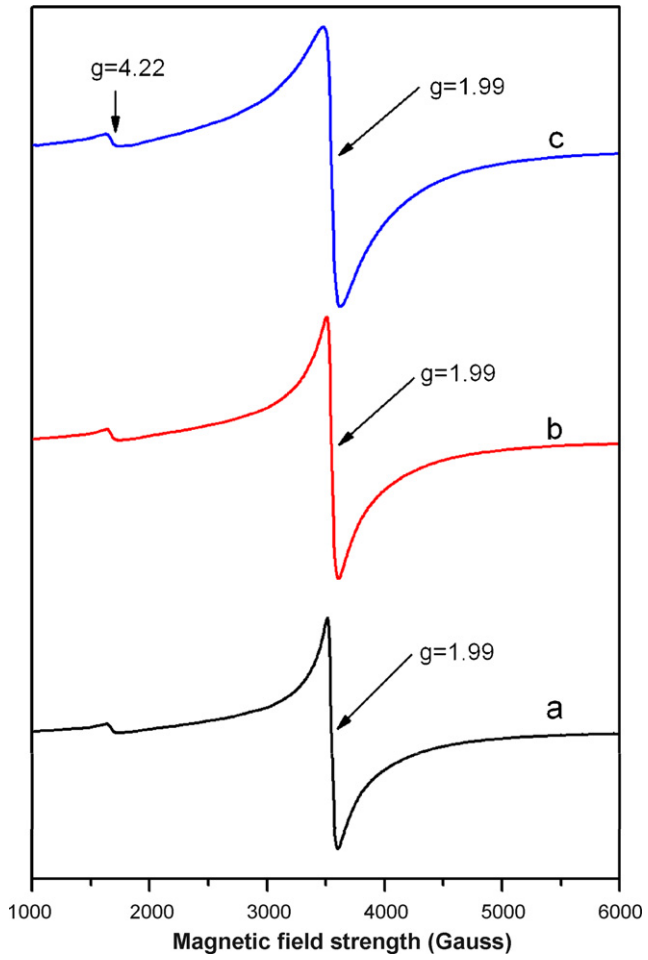

Fig. 4. EPR spectra of (a) 0.1% Fe–TiO_2, (b) 0.2% Fe–TiO_2, and (c) 0.4% Fe–TiO_2.

that in Fe_2O_3 (710.7 eV for $2p_{3/2}$) [29], probably indicative of more positively charged surface Fe^{3+}. The positive shift of Fe 2p level binding energy may be due to the diffusion of Fe^{3+} into TiO_2 lattice and the formation of Fe–O–Ti bond in the sample.

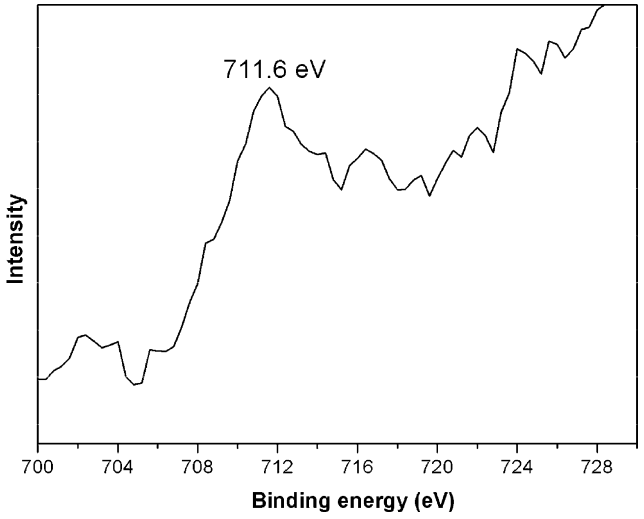

Fig. 5. XPS spectrum of Fe 2p peak of sample 0.4% Fe–TiO_2.

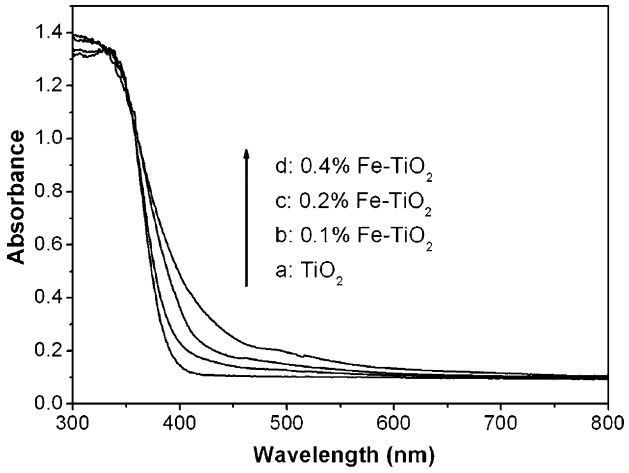

Fig. 6. UV–vis DRS of (a) TiO_2, (b) 0.1% Fe–TiO_2, (c) 0.2% Fe–TiO_2, and (d) 0.4% Fe–TiO_2.

3.4. UV–vis diffuse reflectance spectra

The optical absorption properties of undoped TiO_2 and Fe–TiO_2 samples were examined with UV–vis diffuse reflectance spectra (DRS) and the representative results are shown in Fig. 6. For the undoped TiO_2, an absorption edge rising steeply toward the UV below 387 nm can be attributed to band-gap excitation of anatase (~3.2 eV). Undoped TiO_2 has no absorption in visible region (>400 nm), whereas Fe–TiO_2 samples exhibit a red shifts of absorption edge and a significant enhancement of light absorption at a wavelength of 400–600 nm. The light absorption in the range from 400 to 600 nm increases with increasing the Fe content in Fe–TiO_2, accompanied with the changes on color from white to reddish yellow. According to the previous reports [11,24], the presence of metal ions in TiO_2 does not modify the position of the valence band edge of TiO_2. Instead, it introduces new energy levels (Fe^{3+}/Fe^{4+}) of the transition metal ions into the band gap of TiO_2. Therefore, the absorption edges shift toward longer wavelengths for the Fe-doped TiO_2 should come from the electronic transition from the dopant energy level (Fe^{3+}/Fe^{4+}) to the conduction band of TiO_2.

The direct band gap energy for Fe–TiO_2 can be estimated from a plot of $(\alpha h\nu)^2$ versus photon energy ($h\nu$). The intercept of the tangent to the plot will give a good approximation of the band gap energy for Fe–TiO_2. The absorption coefficient α can be calculated from the measured absorbance (A) according to the Refs. [30,31]. The band gap energies estimated from the intercept of the tangents to the plots are 3.20, 3.10, 3.02 and 2.89 eV for different doping concentration at 0, 0.1, 0.2, and 0.4%, respectively.

3.5. Photocatalytic activity and mechanism analysis

The photocatalytic activity of undoped TiO_2 and Fe–TiO_2 samples was determined by the photocatalytic degradation of MO. MO was selected as a model pollutant because it is a common contaminant in industrial wastewater and cannot be photodegraded in the absence of photocatalyst under light irradiation. As is well known, the photodegradation rate of MO is relative to the pH value of reaction solution. But in our experiments, all the solutions for photocatalytic reaction were in weak acid condition and no evident changes of pH were found. The constancy of pH value may ascribe to the generation of aminocontaining products from dimethyl amino- and azo-groups (Scheme 1). In very low concentration, those amino-containing products might neutralize the generated hydrosulfate ions, and thus stabilize the pH value.

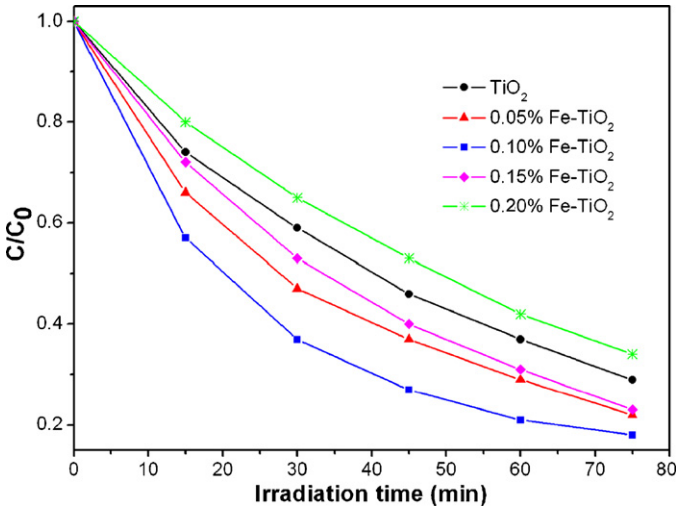

Fig. 7. Photodegradation of MO by undoped TiO_2 and Fe–TiO_2 catalysts as a function of UV light irradiation time.

The representative photodegradation curves for Fe–TiO_2 samples under UV and visible light irradiation are shown in Figs. 7 and 8, respectively. In the two Figs, C_0 and C are the initial concentration of MO before and after light irradiation, respectively. It was found that Fe^{3+} doping influences the photocatalytic activity under both UV and visible light irradiation. At the beginning, the photocatalytic activity of the catalysts increases with the increase of Fe^{3+} content in TiO_2, and then has a downtrend with further increasing the Fe^{3+} content. Under UV light irradiation, the optimal doping levels of Fe^{3+} is 0.1%, while

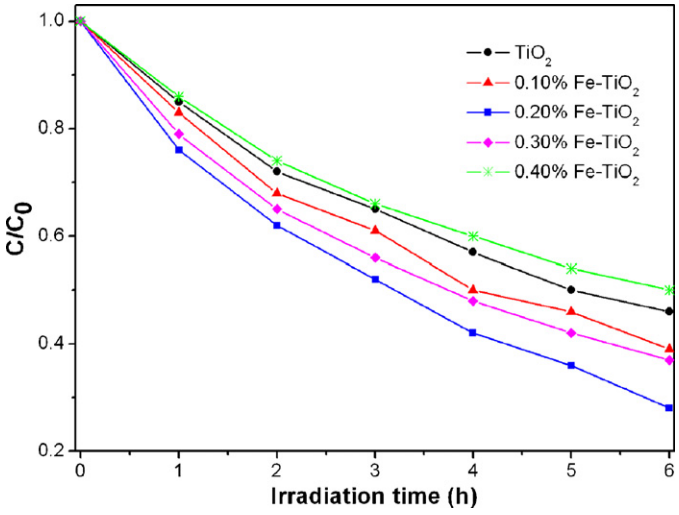

Fig. 8. Photodegradation of MO by undoped TiO_2 and Fe–TiO_2 catalysts as a function of visible light irradiation time.

0.2% is the optimal Fe^{3+} doping content for the degradation of MO under visible light irradiation. Under UV light irradiation, only sample 0.10% Fe–TiO_2 exhibits more photoactive than P25, while all of the samples, 0.05% Fe–TiO_2, 0.1% Fe–TiO_2, 0.15% Fe–TiO_2, 0.2% Fe–TiO_2, and 0.3% Fe–TiO_2 are more photoactive than P25 under visible light irradiation (Table 1). The different results reveal that the photoactive enhancement mechanisms under UV and visible light irradiation are different.

From Fig. 2 and Table 1, it can be found that Fe doping almost has no influences on the crystal structure and morphology of the obtained samples. Although Fe doping affects the crystal size and specific surface area (S_{BET}) of the samples to a certain extent, the photocatalytic activity of the catalysts is not in accordance with the variations of crystal size and S_{BET}. The effect of Fe^{3+} doping on the photocatalytic activity under UV light irradiation should be due to the reason that an appropriate amount of Fe^{3+} ions can act as intermediates for photo-generated holes and electrons transfer, and inhibit the recombination of holes and electrons.

Due to the facts that the energy level for Fe^{3+}/Fe^{4+} is above the valence band edge of TiO_2 and the energy level for Fe^{3+}/Fe^{2+} is below the conduction band edge of TiO_2 [27], Fe^{3+} ions, acting as both electrons and holes traps, can turn into Fe^{2+} and Fe^{4+} ions by trapping photo-generated electrons and holes traps, respectively (Eqs. (3) and (4)). According to the viewpoint of crystal field theory [17], Fe^{2+} and Fe^{4+} ions are relatively unstable when compared to Fe^{3+} ions, which have half-filled $3d^5$ orbital. Therefore, the trapped charges can easily release from Fe^{2+} or Fe^{4+} ions and then migrate to the surface to initiate the photocatalytic reaction. Fe^{2+} ions can be oxided to Fe^{3+} ions by transferring electrons to absorbed O_2 on the surface of TiO_2 (Eq. (5)) or a neighboring surface Ti^{4+} ions (Eq. (6)). Meanwhile, the adsorbed O_2 is reduced to O_2^- (Eqs. (5) and (7)), which can further degrade MO (Fig. 9). Similarly, Fe^{4+} ions also are reduced to Fe^{3+} ions by releasing electrons, while surface hydroxyl group translates into hydroxyl radical (Eq. (8)). As a result, the introduction of appropriate Fe^{3+} ions is responsible for the reduction of the photo-generated hole–electron recombination rate and favors the improvement of photocatalytic activity:

$$TiO_2 + h\nu \rightarrow e^- + h^+ \quad (2)$$

$$Fe^{3+} + h^+ \rightarrow Fe^{4+} \quad (3)$$

$$Fe^{3+} + e^- \rightarrow Fe^{2+} \quad (4)$$

$$Fe^{2+} + O_2(ads) \rightarrow Fe^{3+} + O_2^- \quad (5)$$

$$Fe^{2+} + Ti^{4+} \rightarrow Fe^{3+} + Ti^{3+} \quad (6)$$

$$Ti^{3+} + O_2(ads) \rightarrow Ti^{4+} + O_2^- \quad (7)$$

$$Fe^{4+} + OH^-(ads) \rightarrow Fe^{3+} + OH^\bullet(ads) \quad (8)$$

However, when the concentration of Fe^{3+} ions becomes too large, Fe^{3+} ions can act as the recombination centers for the photo-generated electrons and holes (Eqs. (3), (4) and (9)–(11)), resulting in the decrease of photocatalytic activity. In our case the optimal doping concentration is 0.1%. Above that concentration, Fe^{3+} ions steadily become recombination centers and the photocatalytic activity gradually decreases:

$$Fe^{4+} + e^- \rightarrow Fe^{3+} \quad (9)$$

$$Fe^{2+} + h^+ \rightarrow Fe^{3+} \quad (10)$$

$$Fe^{2+} + OH^\bullet \rightarrow Fe^{3+} + OH^- \quad (11)$$

Different with the intrinsic excitation of TiO_2 under UV irradiation, the excitation behavior of Fe–TiO_2 under visible irradiation arises from the electronic transition from the dopant energy level (Fe^{3+}/Fe^{4+}) to the conduction band of TiO_2. Due to the fact that the t_{2g} level of 3d orbital of Fe^{3+} ion is above the valence band of TiO_2, Fe^{3+} ion can absorb a photon with a wavelength exceeding 400 nm to produce a Fe^{4+} ion and a TiO_2 conductive band electron. The conductive band electron further reacts with adsorbed O_2 to form O_2^-, while Fe^{4+} reacts with surface hydroxyl group to produce hydroxyl radical. Thus, MO was photodegraded even under the visible light irradiation (Fig. 9):

$$Fe^{3+} + h\nu \rightarrow Fe^{4+} + e^- \quad (12)$$

$$e^- + O_2(ads) \rightarrow O_2^- \quad (13)$$

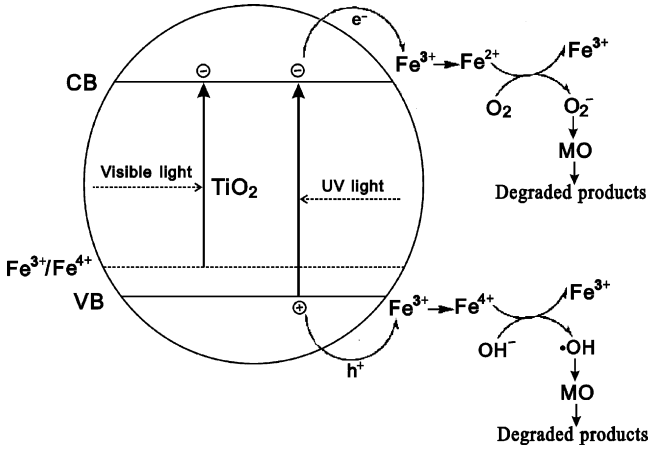

Fig. 9. Proposed mechanism for MO degradation under UV and visible light irradiation.

4. Conclusions

With the present methodology, involving controlled hydrolysis and hydrothermal treatment, TiO_2 microspheres with anatase crystal phase can be prepared. The presence of macro-/mesoporous structure should facilitate the pass of reactants and products and consequently favor the improvement of photocatalytic activity. EPR results confirm that Fe^{3+} ions can be successfully incorporated into the crystal lattice of TiO_2 with the present preparation method. The optimal doping Fe^{3+} concentrations under UV light irradiation and visible light irradiation were 0.1 and 0.2%, respectively. Under UV light irradiation, appropriate Fe^{3+} doping can efficiently separate the photo-generated electrons and holes and consequently improve the photocatalytic activity, whereas excess Fe^{3+} also can become the recombination centers for the photo-generated electrons and holes, leading to

the decrease of photocatalytic activity. Under visible light irradiation, Fe^{3+} doping introduces a new energy level (Fe^{3+}/Fe^{4+}) above the valence band, resulting in the enhancement of light absorption in visible light regions and the improvement of photocatalytic activity.

Acknowledgements

This work has been supported by Program for New Century Excellent Talents in University (NCET-04-0414); Shanghai Nanotechnology Promotion Centre (0652nm045, 0752nm001), National Nature Science Foundation of China (2057709, 20773039), the National Basic Research Program of China (2004CB719502, 2007CB613306) and the Ministry of Science and Technology of China (2006AA06Z379, 2006DFA52710). A part of research work was finished in Shanghai Nanotechnology Joint Lab.

References

[1] A. Fujishima, K. Honda, Electrochemical photolysis of water at a semiconductor electrode, Nature 238 (1972) 37–38.
[2] A. Fujishima, T.N. Rao, D.A. Truk, Titanium dioxide photocatalysis, J. Photochem. Photobiol. C: Photochem. Rev. 1 (2000) 1–21.
[3] G.Q. Li, C.Y. Liu, Y. Liu, Different effects of cerium ions doping on properties of anatase and rutile TiO_2, Appl. Surf. Sci. 253 (2006) 2481–2486.
[4] M.I. Litter, Heterogeneous photocatalysis: transition metal ions in photocatalytic systems, Appl. Catal. B: Environ. 23 (1999) 89–114.
[5] H. Yamashita, M. Harada, J. Misaka, M. Takeuchi, B. Neppolian, M. Anpo, Photocatalytic degradation of organic compounds diluted in water using visible light-responsive metal ion-implanted TiO_2 catalysts: Fe ion-implanted TiO_2, Catal. Today 84 (2003) 191–196.
[6] J.F. Zhu, W. Zheng, B. He, J.L. Zhang, M. Anpo, Characterization of Fe–TiO_2 photocatalysts synthesized by hydrothermal method and their photocatalytic reactivity for photodegradation of XRG dye diluted in water, J. Mol. Catal. A 216 (2004) 35–43.
[7] X.W. Zhang, M.H. Zhou, L.C. Lei, Co-deposition of photocatalytic Fe doped TiO_2 coatings by MOCVD, Catal. Commun. 7 (2006) 427–431.
[8] M. Anpo, M. Takeuchi, The design and development of highly reactive titanium oxide photocatalysts operating under visible light irradiation, J. Catal. 216 (2003) 505–516.
[9] H. Kato, A. Kudo, Visible-light-response and photocatalytic activities of TiO_2 and $SrTiO_3$ photocatalysts codoped with antimony and chromium, J. Phys. Chem. B 106 (2002) 5029–5034.
[10] J.F. Zhu, Z.G. Deng, F. Chen, J.L. Zhang, H.J. Chen, M. Anpo, J.Z. Huang, L.Z. Zhang, Hydrothermal doping method for preparation of Cr^{3+}–TiO_2 photocatalysts with concentration gradient distribution of Cr^{3+}, Appl. Catal. B 62 (2006) 329–335.
[11] W. Choi, A. Termin, M.R. Hoffmann, The role of metal ion dopants in quantum-sized TiO_2: correlation between photoreactivity and charge carrier recombination dynamics, J. Phys. Chem. 98 (1994) 13669–13679.
[12] Y.H. Zhang, S.G. Ebbinghaus, A. Weidenkaff, T. Kurz, H.A. Krug von Nidda, P.J. Klar, M. Güngerich, A. Reller, Controlled iron-doping of macrotextured nanocrystalline titania, Chem. Mater. 15 (2003) 4028–4033.
[13] J.A. Navío, G. Colón, M.I. Litter, G.N. Bianco, Synthesis, characterization and photocatalytic properties of iron-doped titania semiconductors prepared from TiO_2 and iron(III) acetylacetonate, J. Mol. Catal. A 106 (1996) 267–276.
[14] J. Lin, Y. Lin, P. Liu, M.J. Meziani, L.F. Allard, Y.P. Sun, Hot-fluid annealing for crystalline titanium dioxide nanoparticles in stable suspension, J. Am. Chem. Soc. 124 (2002) 11514–11518.
[15] J.G. Yu, M.H. Zhou, H.G. Yu, Q.J. Zhang, Y. Yu, Enhanced photoinduced super-hydrophilicity of the sol–gel-derived TiO_2 thin films by Fe-doping, Mater. Chem. Phys. 95 (2006) 193–196.
[16] C.Y. Wang, C. Bottcher, D.W. Bahnemann, J.K. Dohrmann, A comparative study of nanometer sized Fe(III)-doped TiO_2 photocatalysts: synthesis, characterization and activity, J. Mater. Chem. 13 (2003) 2322–2329.
[17] M.H. Zhou, J.G. Yu, B. Cheng, Effects of Fe-doping on the photocatalytic activity of mesoporous TiO_2 powders prepared by an ultrasonic method, J. Hazard. Mater. 137 (2006) 1838–1847.
[18] K.S.W. Sing, D.H. Everett, R.A.W. Haul, L. Moscou, R.A. Pierotti, J. Rouquerol, T. Siemieniewska, Reporting physisorption data for gas/solid systems with special reference to the determination of surface area and porosity (recommendations 1984), Pure Appl. Chem. 57 (1985) 603–619.
[19] A. Collins, D. Carriazo, S.A. Davis, S. Mann, Spontaneous template-free assembly of ordered macroporous titania, Chem. Commun. (2004) 568–569.
[20] J.G. Yu, L.J. Zhang, B. Cheng, Y.R. Su, Hydrothermal preparation and photocatalytic activity of hierarchically sponge-like macro-/mesoporous titania, J. Phys. Chem. C 111 (2007) 10582–10589.
[21] J.G. Yu, Y.R. Su, B. Cheng, Template-free fabrication and enhanced photocatalytic activity of hierarchical macro-/mesoporous titania, Adv. Funct. Mater 17 (2007) 1984–1990.
[22] A. Vantomme, A. Léonard, Z.Y. Yuan, B.L. Su, Self-formation of hierarchical micro–meso–macroporous structures: Generation of the new concept "hierarchical catalysis", Colloids Surf. A 300 (2007) 70–78.
[23] T.A. Egerton, E. Harris, E.J. Lawson, B. Mile, C.C. Rowlands, An EPR study of diffusion of iron into rutile, Phys. Chem. Chem. Phys 3 (2001) 497–504.
[24] K. Nagaveni, M.S. Hegde, G. Madras, Structure and photocatalytic activity of $Ti_{1-x}M_xO_{2\pm\delta}$ (M = W, V, Ce, Zr, Fe, and Cu) synthesized by solution combustion method, J. Phys. Chem. B 108 (2004) 20204–20212.
[25] M. Graetzel, R.F. Howe, Electron paramagnetic resonance studies of doped titanium dioxide colloids, J. Phys. Chem. 94 (1990) 2566–2572.
[26] Z.H. Yuan, L. Zhang, Influence of $ZnO + Fe_2O_3$ additives on the anatase-to-rutile transformation of nanometer TiO_2 powders, Nanostruct. Mater. 10 (1998) 1127–1133.
[27] Y. Ma, X.T. Zhang, Z.S. Guan, Y.A. Cao, J.N. Yao, Effects of zinc and iron(III) doping of titania films on their photoreactivity to decompose rhodamine B, J. Mater. Res. 16 (2001) 2928–2933.
[28] H.B. Jiang, L. Gao, Enhancing the UV inducing hydrophilicity of TiO_2 thin film by doping Fe ions, Mater. Chem. Phys. 77 (2002) 878–881.
[29] C.D. Wagner, W.M. Riggs, L.E. Davis, J.F. Moulder, G.E. Muilenberg, Handbook of X-ray Photoelectron Spectroscopy, Perkin-Elmer Corporation, Physical Electronics Division, USA, 1979.
[30] C. Kormann, D.W. Bahnemann, M.R. Hoffmann, Preparation and characterization of quantum-size titanium dioxide, J. Phys. Chem. 92 (1988) 5196–5201.
[31] G. Rothenberger, J. Moser, M. Graetzel, N. Serpone, D.K. Sharma, Charge carrier trapping and recombination dynamics in small semiconductor particles, J. Am. Chem. Soc. 107 (1985) 8054–8059.